Nanotechnology

Differently shaped nanocrystalline (Fe,Y)₃O₄ and its adsorption efficiency toward inorganic arsenic species

To cite this article before publication: Biljana Dojinovi *et al* 2019 *Nanotechnology* in press https://doi.org/10.1088/1361-6528/ab3ca2

Differently shaped nanocrystalline $(Fe,Y)_3O_4$ and its adsorption efficiency toward inorganic arsenic species

Biljana P. Dojčinović,[*a,b] Boštjan Jančar,[c] Lotfi Bessais,[d] Aleksandar S. Kremenović,[e] Nataša P. Jović-Jovičić,[a] Predrag T. Banković,[a] Dalibor M. Stanković,[b] Miloš Ognjanović[b] and Bratislav V. Antić[*b]

[a] University of Belgrade, Institute of Chemistry, Technology and Metallurgy, Njegoševa 12, 11000 Belgrade, Serbia

[b] University of Belgrade, The Vinča Institute of Nuclear Sciences, POB 522, 11001 Belgrade, Serbia

[c] Jožef Štefan Institute, Jamova 39, 1000 Ljubljana, Slovenia

[d] Université Paris Est, ICMPE, (UMR7182), CNRS-UPEC, Thiais, F-94320, France

[e] University of Belgrade, Faculty of Mining and Geology, Đušina 7, 11000 Belgrade, Serbia

Abstract

Herein we report effects of partial substitution of Fe^{3+} by Y^{3+} in magnetite (Fe_3O_4) on morphology and inorganic arsenic species adsorption efficiency of the $Fe_{3-x}Y_xO_4$ nanoparticles formed. The series of $Fe_{3-x}Y_xO_4$ (x=0.00, 0.042 and 0.084, labeled as Y00, Y05 and Y10, respectively) was synthesized using co-precipitation followed by microwave-hydrothermal treatment (MW) at 200 °C. With increase of yttrium content (x value), both the morphological inhomogeneity of the samples and the fraction of spinel nanorods as compared to spinel pseudospherical particles increased. By both TEM (transmission electron microscopy) and XRPD (X-ray powder diffraction) analyses, it was determined that the direction of growth of the spinel nanorods is along the [110] crystallographic direction. The $Fe_{3-x}Y_xO_4$ affinities of adsorption toward the inorganic arsenic species, As(III) (arsenite, AsO_3^{3-}) and As(V) (arsenate, AsO_4^{3-}), were investigated. Increased Y^{3+} content related to changes in sample morphology was followed by a decrease of As(III) removal efficiency and vice versa for As(V). The increase in Y^{3+} content, in addition to increasing the adsorption capacity for As(V), significantly expanded the optimum pH range for the maximum removal and decreased the contact time for necessary 50% removal ($t_{1/2}$) of As(V) (Y00: pH 2-3, $t_{1/2}$=3.12 min; Y05: pH 2-6, $t_{1/2}$=2.12 min and Y10: pH 2-10, $t_{1/2}$=1.12 min). The results point to incorporation of Y^{3+} in the crystal lattice of magnetite, inducing nanorod spinel structure formation with significant changes in sorption properties important for the removal of inorganic arsenic from waters.

Keywords: Magnetite, Microstructure, Microwave-hydrothermal synthesis (MW), Adsorption, Arsenic

1. Introduction

Nanoscale magnetite, Fe_3O_4, has attracted considerable interest recently due to its various potential applications, such as nanomedicine, batteries, magnetic storage media, ferrofluid technologies, waste water treatment, etc [1–3]. Also, magnetite is used as an adsorbent to remove toxic elements, mainly coper, arsenic, chromium, and mercury, from waste water [2].

The various methods used for synthesizing nanoscale magnetite lead to formation of nanoparticles with different sizes and morphologies, such as nanospheres, octahedral nanoparticles, nanorings, nanoprisms, nanoplates, nanotubes, nanorods, and nanowires [4]. Synthesis method influences microstructure parameters (microstrain, particle size, morphology, defects) that further determine the physical properties of the materials. Consequently, by selection and control of the synthesis route, it is possible to tailor physical/chemical properties of nanomaterials.

One of the most common routes for synthesizing nano magnetite is co-precipitation. Thanh and co-authors studied in detail the influence of pH, temperature, and reaction time on the morphology and phase composition of the nanomaterials, as well as the reaction mechanism of magnetite formation in a co-precipitation synthesis procedure [5]. It was shown that changing pH in the range of 6-10 caused significant differences in phase composition and size distribution of the prepared samples. The obtained magnetite nanoparticles showed changes in average particle size of about 10 nm per pH unit [5]. In our research, we used co-precipitaion as the first step for sample preparation, and microwave hydrotermal treatment as the second step.

One-dimensional (1D) nanostructure materials (nanotubes, nanofibers, and nanorods) are of particular importance due to their unique physical and chemical properties. Preparation of 1D spinel nanostructures is challenging because the high symmetry of the spinel structure is unfavorable for 1D growth [3, 6]. An inspection of literature data indicate it is possible to obtain Fe_3O_4 nanorods by various methods: a hydrothermal method in the presence of polyethylene glycol [7]; hard and soft template assisted synthesis [3]; transformation of magnetite

nanoparticles to nanorods using alkaline hydrothermal treatment without addition of any polymer templates [8]; thermal decomposition of iron(II) oxalate nanorods [9], and; reversed precipitation of magnetite under magnetic field [10], etc.

The physico-chemical properties of magnetic nanomaterials are significantly modified in comparison with their bulk counterparts. Some new magnetic properties and phenomena, such as superparamagnetism, spin canting and core/shell structure are characteristic only of nanoscale magnetic materials. For small particles, there is a large surface/volume ratio, and thus, a lot of active ions are on the surface. There are fast growing areas of research in the field of nanotechnology related to various applications. Among them, (magnetic) nanoparticles, coated (magnetic) nanoparticles and nanocomposites are being intensively investigated for use in waste water treatment, particularly for arsenic removal from water [11].

Arsenic (chemical formula As, and atomic number 33) is a ubiquitous element, being the 20th most abutant element in the Earth and the 14th in seawater. The usual oxidation states of this element are -3, 0, +3 and +5. This element has wide application in several industries such as semucinductors and agriculture. Despite the variety of practical uses (and its presence in the human body), this element can be considered as an extremely harmful toxin for the human population and environment [12]. High and dangerous concentrations of this element can be found in groundwaters, predominantly those used as drinking water and in agriculture. This is a global problem, as this situation is reported in the USA, Bangladesh, China, Hungary, Serbia, and other countries. Concentrations of arsenic several times higher than allowed were reported in the north of Serbia (Vojvodina), where only 11% of water supply systems have arsenic concentrations lower than 10 μg/L. Due to these facts, removal of arsenic from the water is a highly investigated research field. Different methodologies were reported for efficient removal of arsenic and purufication of water [13]. These techniques are predominantly based on oxidation [14], coagulation [15], ion-exchange [16] and adsorption[17], etc. However, robustness, lack of undue adverse environmental effects, adequate quantity of water production, economical feasibility and safety are required criteria that any one method must meet to be considered for industrial utilization in this field. Arsenic adsorption on the surface of nanomaterials could be a promising methodology and deserves serious investigation as a candidate for arsenic removal [18, 19].

Various nanomaterials have been employed for this purpose [11]. TiO_2-based nanoparticles remove As(V) mainly by adsorption, and As(III) by oxidation to As(V), before adsorption under UV light irradiation, with increase in adsorption capacity of 200-fold over other materials [20]. Martinson et al reported that CuO nanoparticles had adsorption capacities up to 22.6 mg g^{-1} and 26.9 mg g^{-1} for As(V) and As(III), respectively [21]. Flower-like, nanoflakes and nest-like magnesium oxide (MgO) nanostructures have unusually high adsorption capacities [11]. Iron oxide in pure form and doped nanoparticles, such as yttrium-doped iron oxide [22], γ-Fe_2O_3 nanorods [23], and Fe_3O_4 nanoparticles [24] have attracted significant attention as potential sorbents for arsenic removal. To improve adsorption ability towards arsenic, the magnetic materials are generally combined with others, such as activated carbon fiber, chitosan, reduced graphene/graphite oxide, or clay [22], forming magnetic nanocomposite which can be easily removed from the waste water by external magnets.

Many studies showed the possibility to optimize the physical properties of iron oxide by partial substitution of cations with *3d* or *4f* elements, make them promising for a wide range of applications, e.g. [25] The rare earth (*4f*) ions are larger than the hosts, and hence, they often create structural distortions and have significant influence on the crystallite strain. It was a challenge to prepare nanomaterials with the same chemical composition but different morphologies, which would enable study of the effects of morphology on the materials' arsenic adsorption efficiencies. In this paper, we report details of a synthesis procedure used to form nanocrystalline pure and yttrium-substituted magnetite. The influence of substitution level and the temperature on the phase composition, morphology and microstructure parameters of the obtained $Fe_{3-x}Y_xO_4$ samples was investigated. Effects of morpholgy/chemical composition on removal arsenic(III) and arsenic(V) from waste water were tested. Removal efficiencies of the $Fe_{3-x}Y_xO_4$ nanoparticles were studied by measuring contact time, pH range and the influence of competing agents was investigated.

2. Methods

2.1. Synthesis of $Fe_{3-x}Y_xO_4$

The starting compounds were ferrous sulfate heptahydrate (pro analysis, $FeSO_4 \cdot 7H_2O$, Merck, Germany) and ferric chloride hexahydrate (reagent grade, $FeCl_3 \cdot 6H_2O$, Analytika®, Ltd., Czech Republic) and yttrium chloride hexahydrate (pro analysis, $YCl_3 \cdot 6H_2O$, Sigma Aldrich).

Demineralized water (320 mL) was placed in a three-neck flask and deoxygenated for 30 min (in an ultrasonic bath for 15 minutes and 15 min under a stream of N_2). Then, $FeSO_4 \cdot 7H_2O$, $FeCl_3 \cdot 6H_2O$ and $YCl_3 \cdot 6H_2O$ in appropriate stoichiometric ratios ($(Fe^{3+}+Y^{3+}):Fe^{2+}$=0.030:0.015 mol/mol) were dissolved in the deoxygenated water to obtain the series $Fe_{3-x}Y_xO_4$ (x=0.00, 0.05 and 0.10). The mixture was stirred with a mechanical stirrer IKA-Werk, (Janke & Kunkel, RW 20) (400 rpm) in an inert nitrogen atmosphere. After complete dissolution of the salts, 22.5 mL of ammonium hydroxide solution (ACS reagent, 28.0-30.0% NH_3 basis, Sigma Aldrich) was slowly added dropwise at a constant rate. The amount of ammonia was added for 60 minutes at constant stirring. The final pH of the mixture was 10. When the dropwise addition of ammonia finished completely, the mixture was stirred for an additional 15 minutes under N_2 flow. The final, overall volume of the mixture was divided into seven 100 mL PTFE vessels. Each vessel contained 50 mL of the mixture, which was the maximum allowed volume per vessel. Vessels were placed in a HPR-1000/10S high pressure segmented rotor and heated in the microwave digester ETHOS 1 (Advanced Microwave Digestion System, MILESTONE, Italy). The temperature program was designed so the power of microwave irradiation was 0-1000 W, with linear heating of the mixture from room temperature to 200 °C for 10 min. When the temperature of the mixture reached 200 °C, that temperature was maintained for another 10 min. The maximum pressure of the reaction vessels was rated at 100 bars. Following completion of the hydrothermal synthesis assisted by microwave radiation, vessels were quickly cooled in an air flow and the content from all from all was combined in a single glass beaker. The resulting precipitate was washed with demineralized water and separated by an external permanent magnet with decantation of the supernatant. Washing was conducted to obtain negative qualitative reactions to chlorides and sulfates and so conductivity of supernatant was <30 μS/cm. The precipitate obtained after washing was dispersed in 50 mL of water. The synthesized sample was dried at 60 °C. After drying, the residue was triturated in an agate mortar.

The content of Y and Fe in the triturated samples was determined by inductively coupled plasma optical emission spectrometry, ICP-OES (iCAP 6500 Duo ICP, Thermo Fisher Scientific, Cambridge, UK). Elements in solution were quantified after total dissolution of nanomaterials, and they were measured at the following emission wavelengths: Fe II 259.837 nm and Y II 377.433 nm. The results pointed to high substitution levels of the iron in the magnetite with yttrium. Namely, the x values in formula unit $Fe_{3-x}Y_xO_4$ were 0.042 and 0.084 instead of 0.05

and 0.10, respectively, according to the ratio of Fe-/Y- in the starting reaction mixture. Consequently, the chemical composition of the samples with yttrium are $Fe_{2.958}Y_{0.042}O_4$ and $Fe_{2.016}Y_{0.084}O_4$, respectively. Samples with x=0.00, 0.042 and 0.084 were labelled in this paper as Y00, Y05 and Y10, respectively.

2.2. Characterization of $Fe_{3-x}Y_xO_4$

Transmission electron micrographs (TEM) and selected-area diffraction patterns were collected with a Jeol JEM 2100 transmission electron microscope operating at 200 kV for Y05 and Y10 samples. TEM examination for Fe_3O_4 was performed using a FEI Tecnai T20 microscope operating at 200 kV. The samples for analysis were prepared by dispersing the powders in acetone and dropping the suspension on a lacey carbon film supported on a 300-mesh copper grid.

In order to refine the crystal structure and determine the crystallite size and strain, X-ray powder diffraction (XRPD) data for all three samples were collected on a PANalytical X'pert PRO MPD diffractometer in reflection mode using $CuK_{\alpha 1,2}$ radiation. The data were collected in the 2θ range from 10 to 120 º in steps of 0.04 º and with exposition of 10 s per step.

The X-ray line-broadenings were analyzed according to Fullprof [26, 27]. The X-ray line broadenings were studied through refinement of the Thompson Cox Hastings-pseudo Voight (TCH-pV) function parameters and refinement of the multipolar functions, i.e., symmetrized cubic harmonics [28, 29]. Details of the applied models can be found elsewhere [26, 27]. For the instrumental broadening correction, LaB_6 standard specimen was used [30]. The XRPD pattern of the standard (*U*= 0.016363; *V*= -0.024199; *W*= 0.014680; *X*= 0.07221; *Y*= 0.008419; S_L= 0.02480; D_L= 0.02480) was fitted by convolution to the experimental TCH-pV function. Magnetic measurements M(H) were performed on a SQUID magnetometer at room temperature up to a field of ±5T.

Nitrogen adsorption/desorption isotherms were determined using a Sorptomatic 1990 Thermo Finnigan at -196 °C. The samples were outgassed at 160 °C during 20 h. The procedure and used models are described elsewhere, in particular, for those regarding the cumulative pore volume and mesopore region textural properties in Banković *et al.* [31] and for micropore region related data in Žunić *et al.* [32] Data analysis was performed using the Advanced Data Processing 5.1 software.

Hysteresis loops were measured at room temperature on the MPMS XL-5 SQUID magnetometer.

2.3. Adsorption activity for inorganic As(III) and As(V) species

Solutions and instruments. Two separate stock solutions of inorganic arsenic species As(III) (arsenate, AsO_4^{3-}) and As(V) (arsenite, AsO_3^{3-}), each 100 mg/L, were prepared by dissolving appropriate quantities of sodium arsenate dibasic salt heptahydrate ($Na_2HAsO_4 \cdot 7H_2O$, ≥98.0%, Sigma-Aldrich, USA) and arsenic(III) oxide (As_2O_3, 99.8%, Carlo Erba, Italy) in 0.01 M sodium hydroxide, respectively. Solutions of required lower concentrations were prepared by diluting the stock solutions. All solutions were prepared using deionized water with conductivity ranging between 1.0 and 1.5 μS/cm.

The arsenic concentrations in supernatant after adsorption were determined by ICP-OES (iCAP 6500 Duo ICP, Thermo Fisher Scientific, Cambridge, UK). The concentration of arsenic was measured on the emission wavelength As I 193.759 nm. Arsenic, plasma standard solution, Specpure®, As 1000 μg/mL (Alfa Aesar GmbH & Co KG, Germany) was used to prepare calibration solutions.

The pH of solutions was measured using a pH monitor (Microcomputer pH-vision 6071, JENCO Electronics. Ltd., Taiwan), combined with the HI-type electrode 1131 (Hanna Instruments WTW GmbH, USA).

Adsorption experiments. The adsorption of As(III) and As(V) on nanoparticles Y00, Y05 and Y10 was investigated in aqueous solutions in a batch system at room temperature (25 °C) with respect to contact time, pH and competing agents. All adsorption processes were investigated using As(III) or As(V) solutions with initial concentrations of 1000 μg/L. Ionian strength was adjusted in all dilute solutions by the addition of solid NaCl to a final concentration of 0.01 M NaCl. The experiments were carried out in a thermostated shaker (Memmert WNE 14 and SV 1422) using equal volumes of the adsorbate solution V=50.0 mL and mass of adsorbents m_{ads}=25.0 mg (equivalent to 500 mg/L). After adsorption, the suspension was centrifuged (Centrifuge LC-320, Tehtnica, Železniki, Slovenia) at 5000 rpm for 10 min.

Samples were withdrawn from the shaker at predetermined periods of contact time (3, 5, 10, 15, 20, 25, 30, 35, 45, 60, 120, 180, 300, 720, 1440 and 2880 min) at pH 8.0 ± 0.2. The amount

of adsorbed pollutant q_t collected onto tested adsorbents (μg/g) during the time t (min) was calculated using the following mass balance relationship:

$$q_t = \frac{(C_0 - C_t) \cdot V}{m_{ads}}$$

where: C_0 and C_t (μg/L) are initial concentration and concentration of As(III) or As(V) after adsorption time (t), m_{ads} is mass of adsorbent, V is volume of the adsorbate solution.

The pH impact on the adsorption process was investigated using pH range 2-12 and a contact time of 120 min. The influence of anions commonly present in natural waters (sulfate, phosphate and humic acid sodium salt) on arsenic species adsorption on the investigated nanomaterials was studied. The experiment was conducted using anion concentrations of 1 mg/L and 5 mg/L in solutions of As(III) and As(V) at pH 8.0 ± 0.2 and contact time of 120 min.

3. Results and disscusion

3.1. Microstructure analysis

The phase composition and crystal structure of the prepared samples, Y00, Y05 and Y10, were investigated by ICP-OES, EDX, XRPD, TEM and SAED. Diffraction data indicated that all samples crystallized in the spinel type structure, space group $Fd\bar{3}m$. A small amount, less than 1%, of other phases were detected in diffraction patterns for all three samples. This will be discussed in detail in the next sections.

TEM (Fig. 1) revealed that Fe_3O_4 (Y00) particles are pseudospherical with mean particle size of ~ 30 nm. Analysis of TEM micrographs of Y05 showed that particles with different morphologies were formed: predominantly pseudo-spherical particles with mean diameter of about 50 nm and nanorods with mean length of ~80 nm and width of ~11 nm (Fig. 1). In the case of Y10, a larger quantity of nanorods was formed in comparison with Y05. The widths of the Y10 rods were ~10 nm, similar to the Y05 rods, but mean length was shorter, at ~65 nm. Pseudo-spherical particles of Y10 were of diameter ~15-20 nm, and they formed aggregates sized 50-120 nm. Analysis of size distribution of spinel structured nanoroads in Y05 and Y10 samples is shown at Fig. S1-S2 (Supplementary material).

In order to check the chemical composition of pseudospherical and rod-shaped particles of Y10, EDS analysis was performed. In all in situ EDS measurements, approximately the same Y/Fe

ratio was found. The results indicate formation of two morphologies of particles, nanorods and spheres, with the same chemical composition, and point to the influence of partial substitution of Fe^{3+} by Y^{3+} on 1D growth of the nanoparticles, particle morphology, and size. Particles with nanorod morphology in the Y10 sample were investigated in more detail.

Selected-area electron diffraction (SAED) images of an individual Y10 nanorod (Fig. 2a and Fig. 2b) indicates its single crystalline nature. The indexed planes confirm the spinel structure type. Simulation of the experimental data shows the growth direction of spinel nanorods is in the [110] crystallographic direction (Fig. 2c). It is worth mentioning some literature data that point to the influence of synthesis method and substituent on morphology of magnetite-based nanoparticles. Zhen *at al.* [6] studied the influence of Mn^{2+} incorporation in magnetite. They found that only full replacement of Fe^{2+} in magnetite with formation of Mn-ferrite resulted in formation spinel nanorods using a surfactant-free hydrothermal route [6]. After inspection of the literature, we found formation of nanorods in dysprosium-substituted magnetite [33]. In the case of yttrium-substituted magnetite ($Y_xFe_{3-x}O_4$, x=0.00, 0.10, 0.15, 0.20 and 0.40), only spherical nanoparticles were synthesized via a hydrothermal reduction route in the presence of citric acid [3].

It is known that nanoparticles' size and morphology depend on various parameters, such as initial substances in the synthesis reaction, pH, reaction temperature, and time. Consequently, the influence of thermal treatment on formation of our Y10 sample was investigated. The Y10 material was additionally prepared at 120 °C and 160 °C, keeping the remaining parameters as previously used during the synthesis at 200 °C. The mechanism of magnetite growth in a co-precipitation route was investigated earlier by the use of a weak base to enable slow precipitation of the nanoparticles [5]. It was found that precipitate was firstly composed only of α-FeOOH, but after some time, both goethite and magnetite coexisted, and finally, goethite nanoparticles were completely transformed into magnetite [5]. Y^{3+} probably influences the goethite formation phase at first, and geothite transforms, with increasing reaction temperature, into the spinel type nanorods. The intensity of goethite reflections which were measured in diffraction patterns of Y10 samples prepared at 120 °C, 160 °C and 200 °C supported this previous conclusion (Supplementary materials, Fig. S3).

The reaction mechanism was additionaly analyzed by SAED. TEM micrographs show show high yield of rod-shaped nanoparticles in both samples, shown in Fig. 3. SAED analysis of

typical areas with nanorods points to goethite formation phase, with transformation into the spinel rod-shape phase in samples prepared at 160 °C and 200 °C. However, a small quantity of goethite can be expected in the sample prepared at 160 °C, and even less in the sample prepared at 200 °C, accoording our XRPD result.

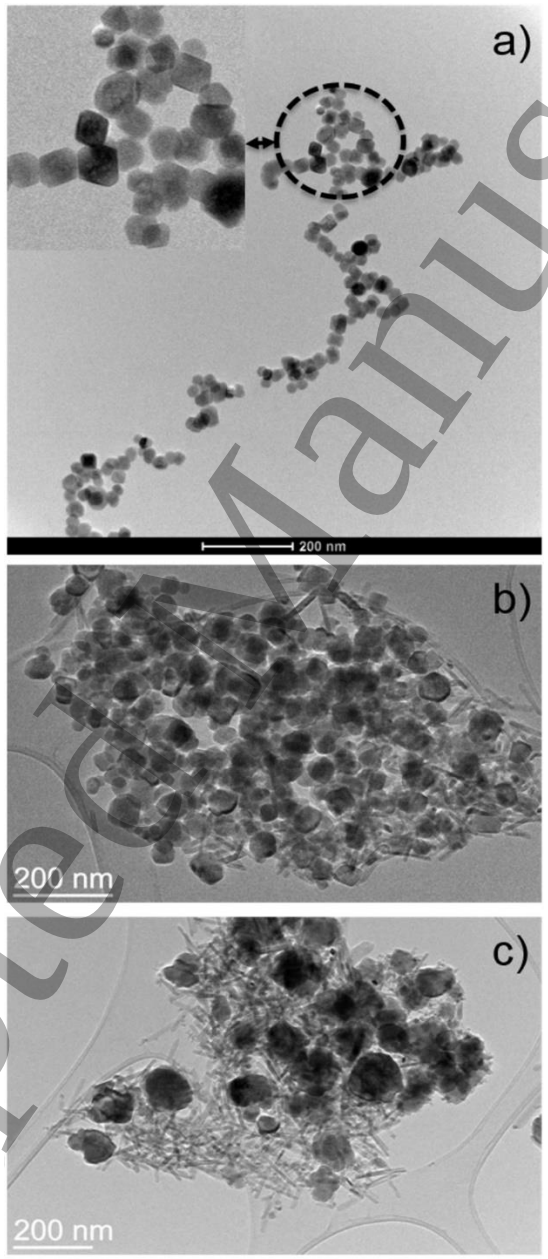

Fig. 1 TEM micrographs of Y00 (a), Y05 (b) and Y10 (c) samples obtained at 200 ºC. Nanorods can be observed in sample Y05, and they are clearly visible in sample Y10.

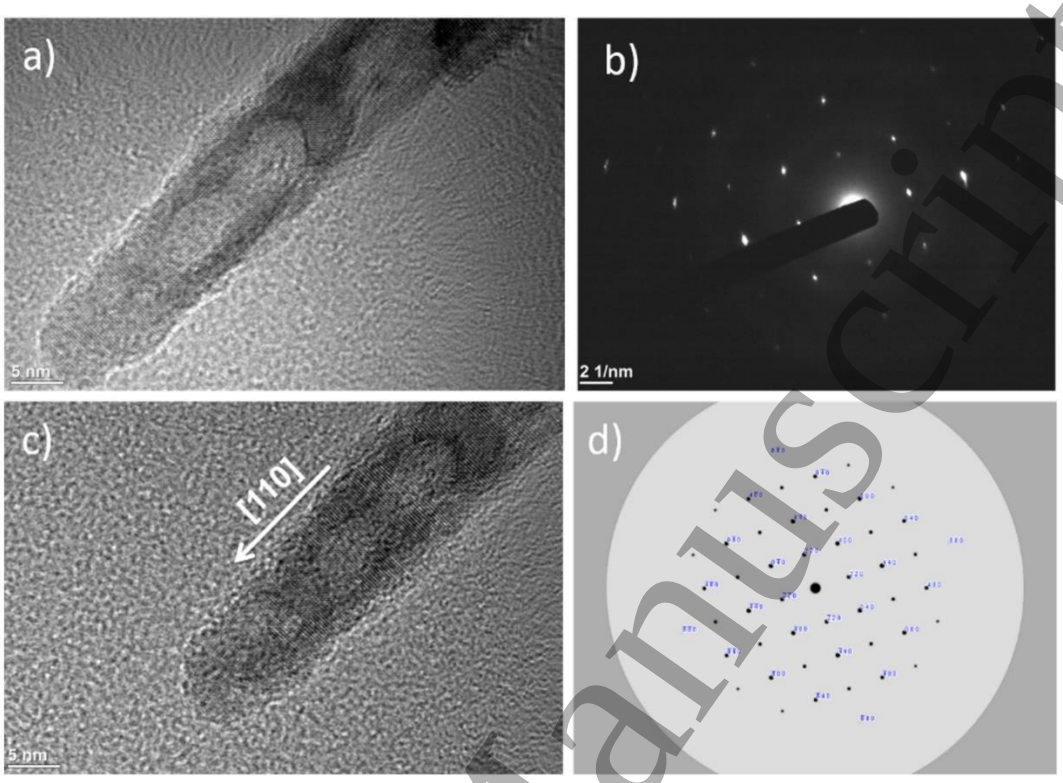

Fig. 2 Experimental (b) and simulated (d) SAED pattern for nanorod (a) and (c) from sample Y10, according to $Y_{0.12}Fe_{2.88}O_4$: ICSD # 249050 z =[00-1].

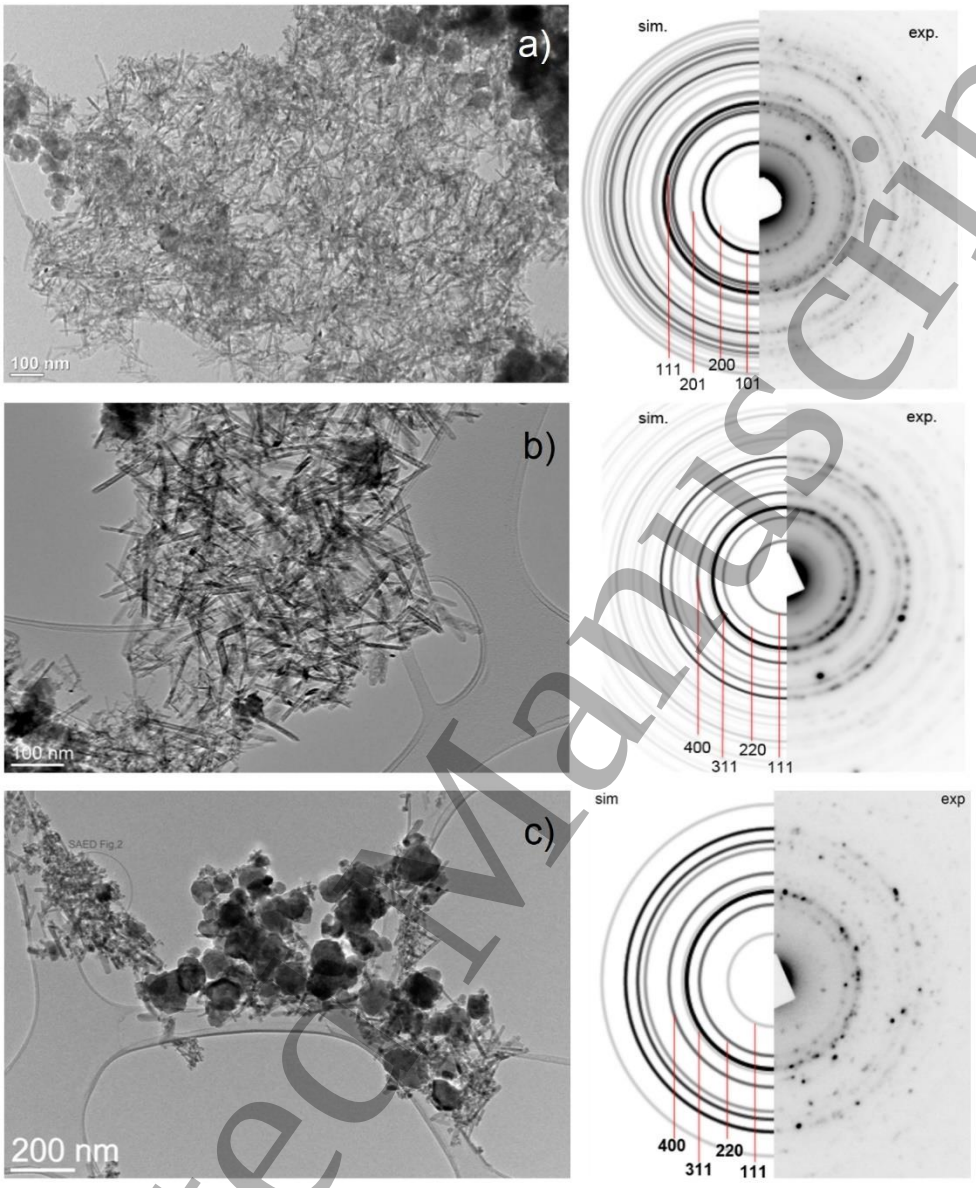

Fig. 3 a) TEM micrographs of Y10 treated at 120 ºC (left) and experimental and simulated SAED patterns according to FeOOH: PDF #: 04-015-8206 (right), b) and c) TEM micrographs of Y10 treated at 160 ºC and 200 ºC, respectively (left) and SAED experimental and simulated according to $Y_{0.15}Fe_{2.85}O_4$: PDF #: 04-014-1397 (right).

3.2. Crystal structure and XRPD line broadening analysis

The collected XRPD data were used to refine structural and microstructural parameters (crystallite size and strain) of the samples prepared at 200 °C. The refinement was performed with the program Fullprof, which enables simultaneous refinement of both the structural and

microstructural parameters, such as: lattice parameters, atomic coordinates, site-occupancies, thermal parameters, crystallite size, and strain. The background intensity of each pattern was refined using linear interpolation between selected points. Refinements continued until convergence was reached. Refined crystal structure and microstructure parameters are given in Table 1. Fig. 4a-c show good agreement between experimental data and structure models. A very small amount (less than 1%) of FeO(OH) in the forms of goethite and lepidocrocite was found in all three samples (characteristic peaks in XRPD patterns at about 2θ: 21.14°, 33.15°, 37.96°, 59.00°, 61.11°). This information was neglected during the refinement process because low crystalline FeO(OH) is at the edge of detection.

Table 1. Crystal data and corresponding agreement factors for investigated specimens

Crystal system: **Face centered cubic**	**Space group: Fd $\bar{3}$ m (227)**		
Composition	**Fe_3O_4**	**$Fe_{2.958}Y_{0.042}O_4$**	**$Fe_{2.016}Y_{0.084}O_4$**
Lattice parameter a (Å)	8.36488(8)	8.3770(1)	8.3905(1)
Cation-anion distance d (Å)			
$d(M_{8a}\text{-}O)x4$	1.884(3)	1.859(3)	1.863(3)
$d(M_{16d}\text{-}O)x6$	2.050(3)	2.069(3)	2.071(3)
Agreement factors			
cR_p (%)	7.36	9.19	9.39
cR_{wp} (%)	10.2	12.2	12.4
R_B (%)	6.91	8.34	8.82
χ^2	8.25	12.9	12.5
Average apparent size* [Å]	183(16)	1886(535)	1641(662)
Average mixing strain* $\cdot 10^4$	8(3)	18(2)	14.3(1)

*-The standard deviations appearing in the global average apparent size and strain are calculated using the different reciprocal lattice directions, and therefore, they can be considered as a measure of the degree of anisotropy and not of the estimated error.

The samples were refined in space group Fd $\bar{3}$ *m*, assuming a spinel type structure with Fe atoms in the special Wyckoff positions 8a and 16d, Y^{3+} in the special Wyckoff position 16d, and O in position 32e. The starting model for determining cation distributions was based on site preferences for cation sites in a spinel structure. Iron ions have no preferences and could occupy both sites (8a and 16d). In all known compounds, Y^{3+} has been found to be octahedrally

coordinated.[26] Linear dependence between unit cell parameter and concentration of Y^{3+} expressed as, a = (8.3646±0.0005) + (0.256±0.008)·x, as x in $Fe_{3-x}Y_xO_4$ showed that Y^{3+} is part of the spinel structure, i.e. synthesis was succsessful. Interatomic distances, obtained from refined atomic coordinates, were used to calculate cationic distributions: $(Fe^{2+}_{0.07}Fe^{3+}_{0.93})_{8a}[Fe^{2+}_{0.93}Fe^{3+}_{1.07}]_{16d}O_4$, $(Fe^{3+)}_{8a}[Fe^{2+}_{1.00}Fe^{3+}_{0.87}Y^{3+}_{0.13}]_{16d}O_4$ and $(Fe^{3+}_{1.00})_{8a}[Fe^{2+}_{1.00}Fe^{3+}_{0.75}Y^{3+}_{0.25}]_{16d}O_4$. These ionic radiuses were used: Fe^{2+} in tetrahedral coordination 0.63 Å, Fe^{3+} in tetrahedral coordination 0.49 Å, Fe^{2+} in octahedral coordination 0.78 Å, Fe^{3+} in octahedral coordination 0.645 Å, Y^{3+} in octahedral coordination 0.90 Å and O in tetrahedral coordination 1.38 Å [34].

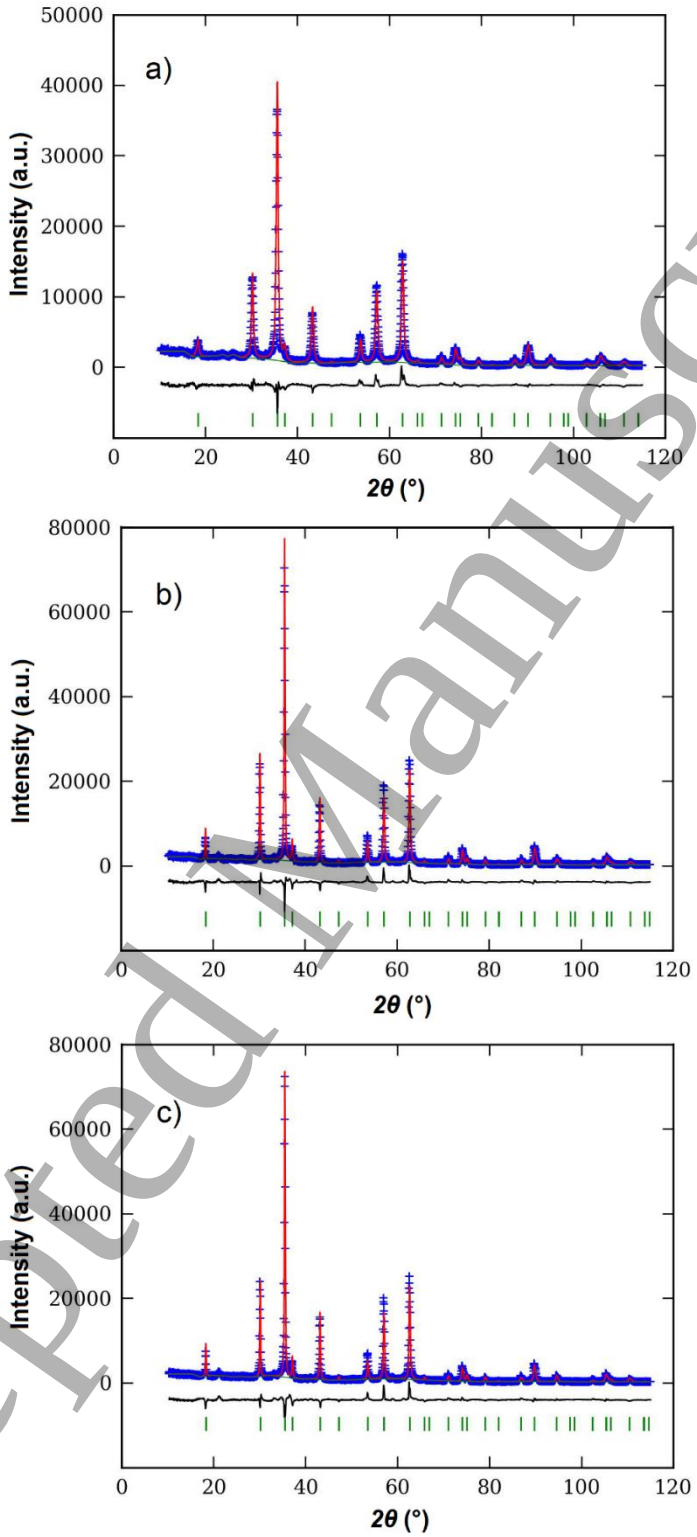

Fig. 4 Final Rietveld plots for: Fe_3O_4 (a), $Fe_{2.958}Y_{0.042}O_4$ (b) and $Fe_{2.916}Y_{0.084}O_4$ (c). Blue crosses denote observed step intensities; the red line represents the corresponding calculated values. The difference curve between observed and calculated values is given at the bottom (black line). Vertical green bars represent peak positions.

As can be seen from Table 2, addition of Y^{3+} provoked increase of apparent strain mixing and crystallite size values. The largest average apparent crystallite size was down the [110] direction for all compositions. With Y^{3+} concentration increase, average apparent crystallite size in the [110] direction was 2-3 times larger than in [100] and [111] directions, as shown in Table 2. This difference was more pronounced with Y^{3+} concentration increase, which is in good agreement with TEM results. For Fe_3O_4, the largest average mixing strain is in the [100] direction and the lowest in the [111] direction. With Y^{3+} concentration increase, the difference in average mixing strain in different directions decreased and was negligible for $Fe_{2.958}Y_{0.042}O_4$.

Table 2. Average apparent crystallite strain and mixing strain in [111], [110] and [100] directions for x= 0.000, 0.042 and 0.084 in $Fe_{3-x}Y_xO_4$.

x	Average apparent crystallite size [Å]	Average mixing strain ($\cdot 10^4$)	Direction
0.000	156	5	[111]
	202	8	[110]
	175	13	[100]
0.042	1440	16	[111]
	3294	18	[110]
	1970	22	[100]
0.084	1090	14	[111]
	3453	14	[110]
	1479	15	[100]

Fig. 5 shows projections of the spherical harmonics describing the size and strain contributions to line profile broadening (GFOURIER[26] incorporated in WINPLOTR[35] was employed to obtain the figures). It should be noted that for the applied Laue class $m\bar{3}m$, all projections on crystal axes are equal. Results on the X-ray line broadening anisotropy of some cubic spinels can be found elsewhere [35, 36].

In order to explain the X-ray line broadening anisotropy, we will discuss the influence of Y^{3+} concentration on the specimen microstructure. The X-ray line broadening anisotropy due to crystallite size effect was significant for all three specimens, including pure Fe_3O_4, and increased

with Y^{3+} concentration increase, Table 1 and Fig. 5. TEM results clearly prove the existence of two nanocrystal morphologies, pseudospheres and nanorods, in all three samples. Moreover, the relative quantity of nanorods increased as Y^{3+} concentration increased. However, in the XRPD patterns, information about these mentioned morphologies is lost, since both posess the same crystal structure and consequently, very similar patterns. Therefore, the crystallite size and strain anisotropy presented here should be interpreted as superposition of the nanorod and pseudoshpere/cubes anisotropies. Having in mind that the relative quantity of nanorods compared to others nanoforms increases as the Y^{3+} concentration increases, crystallite size anisotropy increase is closely connected to nanorod crystallite anisotropy. The crystallite strain anisotropy decreases with nanorod concentration increases, which is an indication that nanorods are characterized by more symmetric strains than pseudosphers/cubes.

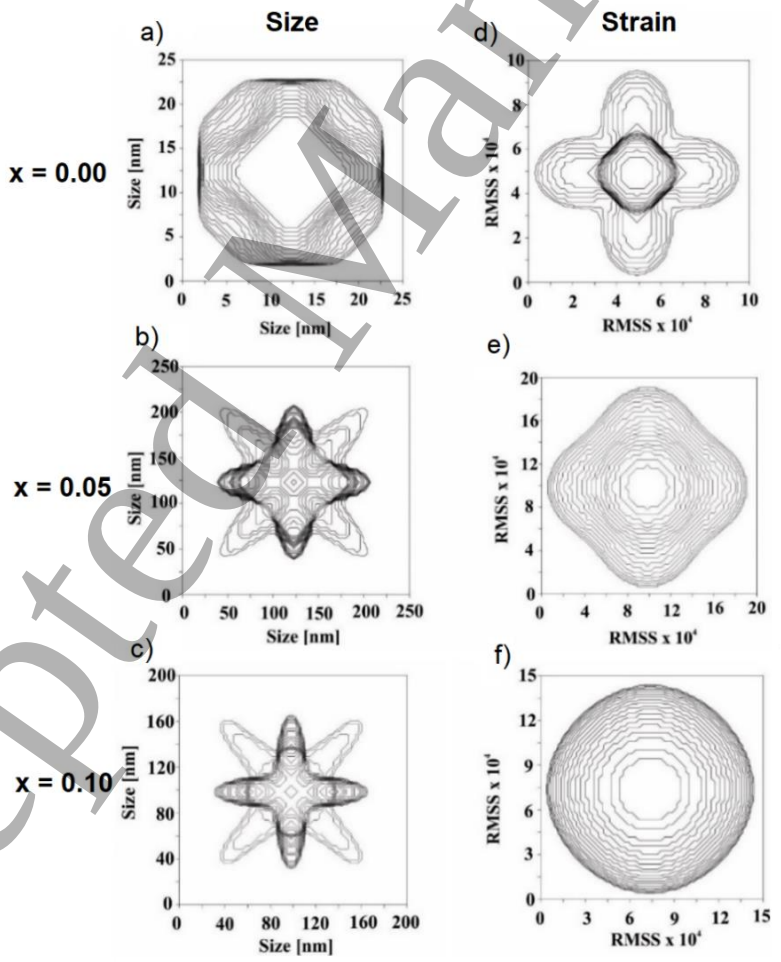

Fig. 5 Projections of the apparent crystallite size and apparent crystallite root mean square strain (RMSS) in the (001) plane for $Fe_{3-x}Y_xO_4$: a) and d) for x = 0.00; b) and e) for x = 0.05; c) and f) for x = 0.10.

3.3. Low-temperature N_2 physisorption analysis of nanocrystalline $Fe_{3-x}Y_xO_4$

To further investigate the nanocrystalline samples, the low-temperature N_2 physisorption method was used. All materials were represented by Type IV isotherms with hysteresis loop of the H1 type (Supplementary materials, Fig. S4–S6). Such isotherms are characteristic of predominantly mesoporous materials, usually industrial adsorbents, that consist of agglomerates or approximately uniform particles in fairly regular arrays, sometimes predominantly spherically shaped [37, 38]. It was found the samples in the current study exhibited low, almost insignificant microporosity, and predominant mesoporosity. Namely, similar values of 2-parameter and 3-parameter equation S_{BET}, as well as application of the t-plot method (Supplementary materials, Table S1), showed the micropore surface area was close to zero. Therefore, the 2-parameter BET method was chosen as the representative one. It was found (Table 3) that total mesopore volume decreases from Fe_3O_4 (Y00) (where the predominant mesopore volume is in pores with diameters of 7.0-19.0 nm, as observed in the Supplementary material, Fig. S7) to Y05 and Y10. The trend in the mesoporous structure was the broadening of pore size distribution toward larger pores from Y00 to Y05 and Y10, while in Y10, significant fractions of smaller diameter mesopores, approaching micropore region diameters, also developed (Supplementary material, Fig. S7–S9). The mesopore surface area in Y10 probably predominantly originates from smaller diameter mesopores. This is due to the fact that S_{BET} was similar for Y00 and Y10, although cumulative pore volume significantly decreased in Y10 in comparison with that of Y00 (Table 3). The observed changes in mesopore diameter parameter values (d_{max} and d_{med}) support that conclusion. These results are also in accordance with the conclusions of our TEM analysis. According to them, the introduction of Y^{3+} led to two separate effects: the occurrence of smaller rod-shaped particles (nanorods) at the expense of the pseudospherical ones, and the increase of average sizes of pseudospherical particles. The greater the Y^{3+} content, the more pronounced the effects. The former effect is responsible for the occurrence of pores with smaller diameters, while the latter results in the increased presence of larger pores. Detected changes in the mesopore surface area are probably due to the combined influence of the two effects, while the decrease in the mesopore volume, V_{mes}, and cumulative pore volume, $V_{0.98}$, from the initial material to the Y^{3+} substituted ones (Table 3), is probably due to the fact that the formation of smaller nanorods is accompanied by decreased presence of the phase with bigger pseudospherical particles. Aside from the changes in pore volume, pore surface area, and pore

size distribution, the low-temperature nitrogen physisorption method could not detect the fact that introducing Y^{3+} into magnetite noticably affected the shape of adsorption/desorption isotherms of the investigated materials.

Table 3. Results (average values) obtained for nitrogen adsorption/desorption experiments

Sample	$S_{BET(2p)}$ [m^2g^{-1}]	$V_{0.98}$ [cm^3g^1]	V_{mes} [$cm^3\ g^{-1}$]	V_{mic} [cm^3g^1]	d_{med} [nm]	d_{max} [nm]
Y00	64	0.199	0.199	0.023	13.8	14.2
Y05	45	0.171	0.172	0.016	18.0	21.2
Y10	62	0.172	0.174	0.022	14.2	9.7

Where: $S_{BET(2p)}$ – specific surface area (2-parameter equation); $V_{0.98}$ – cumulative pore volume (Gurvitch); V_{mic} – micropore volume (Dubinin-Radushkevich), V_{mes} – mesopore volume (Barett-Joyner-Halenda), d_{med} – median mesopore diameter (Barett-Joyner-Halenda) and d_{max} – the most abundant mesopore diameter (Barett-Joyner-Halenda)[38, 39].

3.4. Hysteresis loops

The hysteresis loops of the samples, recorded at 300 K, are shown in Fig. 6. The coercivity field for all samples was close to zero, pointing to the superparamagnetic nature of the samples. The saturation magnetization values, M_S, were estimated by extrapolation of the M vs. $1/H$ curve when $1/H \rightarrow 0$. Fe_3O_4 (Y00) had the largest M_S (74.2 emu/g), while for x=0.10 (Y10) and x=0.05 (Y05), M_S values were found to be 69.2 emu/g and 64.3 emu/g, respectively. Magnetic properties of the samples are influenced by substitution of magnetic Fe^{3+} by diamagnetic Y^{3+}, and by other factors which have to be considered. Results of TEM analysis showed different morphologies in samples containing yttrium, including nanorods and nanospheres. Magnetic properties of 1D nanostructures are influenced by growth direction. The easy magnetization axis is determined by magnetocristalline anisotropy. By TEM analysis, it was found that spinel nanorods grow along the [110] direction, which is one of the easy magnetization axes of magnetite. Literature data for Fe_3O_4 nanowires growing along the [110] axis showed M_S of 35.2–39.5 emu/g [40]. Fe_3O_4 nanowires with [100] growth direction, which is the hard magnetization axis, had a much lower M_S value of 23.0 emu/g [41]. Wang *et al.* reported that nanorods that grow along [111] had high saturation magnetization (90.5 emu/g).[8] Other factors that can influence M_S are crystallite size, size distribution, microstrain, and presence of parasitic phases. Consequently, it is not possible to

give a deep analysis on the influence of each mentioned factor, including yttrium concentration and particle morphology.

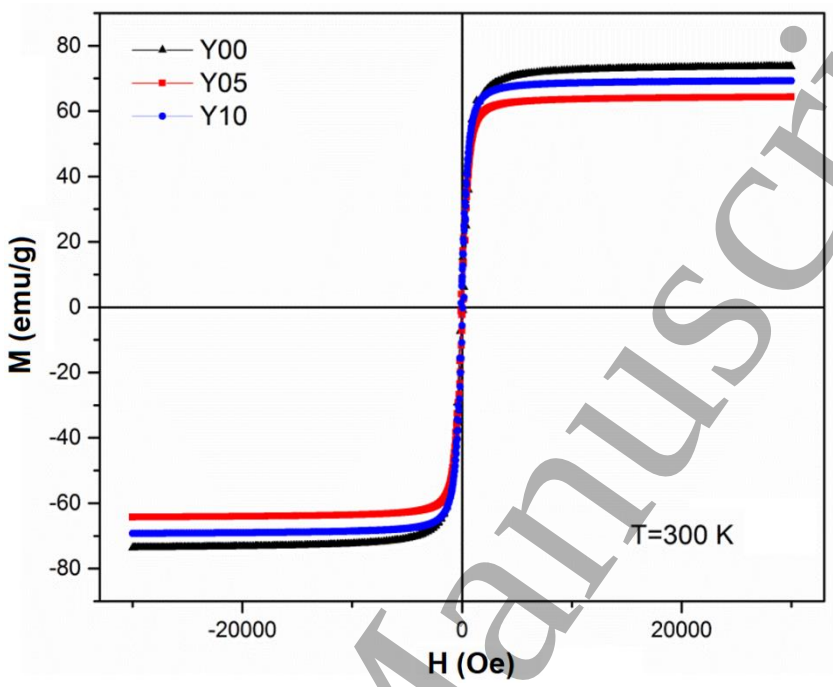

Fig. 6 Hysteresis loops of the samples $Fe_{3-x}Y_xO_4$.

3.5. Adsorption test

In order to determine the equilibrium time for the maximum uptake of As(III) and As(V) the adsorption was monitored with respect to contact time. Additionally, the influences of pH and competing agents were analysed. Removal of inorganic As(III) and As(V) using synthesized materials was investigated.

3.5.1. Effect of contact time

The effect of contact time on the amount of As(III) or As(V) adsorbed on the investigated adsorbents (Y00, Y05 and Y10) are presented in Fig. 7a,b.

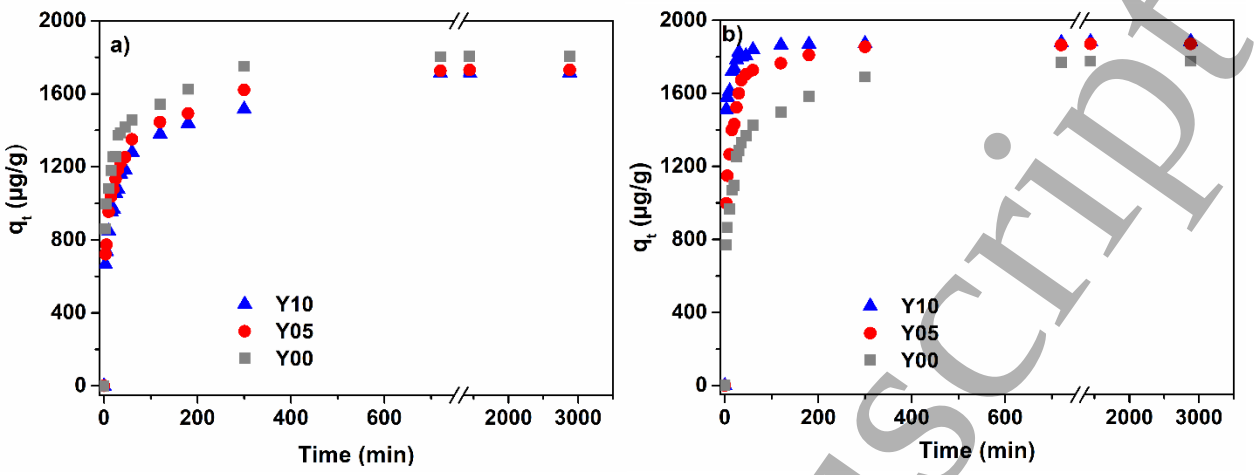

Fig. 7 Effect of contact time on amount of adsorbed a) As(III) and b) As(V) onto adsorbents Y00, Y05 and Y10 (q_t, µg/g); (initial concentration As(III) or As(V) =1000 µg/L; adsorbents= 500 mg/L; pH=8.0±0.2, ionian strength=0.01 M NaCl).

Although more than 70% of the equilibrium amount of As(III), and more than 80% of the equilibrium amount of As(V) was adsorbed within first 60 min, the adsorption of arsenic needed more time to reach equilibrium (Fig. 7a,b). The amounts of As(III) adsorbed after 720 min were higher than after 300 min for the investigated adsorbents, but further extension of contact time had no influence on the amount of adsorbed As(III). Therefore, the equilibrium time was taken as being 720 min. Adsorption of As(V) on Y10 and Y05 was initially high (Fig. 7b), but then, it gradually reached a plateau. The adsorption equilibrium time on Y00 was reached after 720 min, while for Y10 and Y05, it was 180 min earlier. After the equilibrium times, the adsorption time was extended up to 1440 and 2880 min, but desorption under the investigated conditions was not observed.

At the equilibrium times, the amounts of adsorbed As(III) were 1805, 1731 and 1715 µg/g for Y00, Y05 and Y10, respectively. These results indicate that differences in composition and morphology of the samples did not contribute to the amount of adsorbed As(III). In contrast, it seems the amount of adsorbed As(V) could be related to the content of yttrium in samples $Fe_{3-x}Y_xO_4$, since the amounts of As(V) at the equilibrium times were 1777, 1871 and 1884 µg/g for Y00, Y05 and Y10, respectively.

The time, $t_{1/2}$, at which half of total adsorption capacity was reached for As(III) and As(V) adsorption was determined directly from the data and is given in Table 4.

Table 4. The time $t_{1/2}$ for half of total adsorption capacity As(III) and As(V) on Y00, Y05 and Y10

Adsorbent / $t_{1/2}$ (min)	Y00	Y05	Y10
As(III)	3.2	7.4	9.9
As(V)	5.7	3.6	1.3

Generally, all adsorbents had low $t_{1/2}$ times, which indicates fast adsorption processes. The adsorption of As(III) showed higher $t_{1/2}$ times than As(V). The adsorption rates of As(III) and As(V) showed opposite trends. Adsorption of As(III) was faster on sample without Y^{3+}, while the As(V) adsorption rate increased with increasing Y^{3+} content in $Fe_{3-x}Y_xO_4$.

3.5.2. Effect of pH

The distribution of As(III) and As(V) species in aqueous solution strongly depends on pH. In acidic environments (pK_{a1}=2.1), H_3AsO_4 is the dominant form. With increase of pH, the quantity of deprotonated forms, $H_2AsO_4^-$, $HAsO_4^{2-}$ and AsO_4^{3-}, increases according to pKa_2=6.7 and pK_{a3}=11.2. On the other hand, H_3AsO_3, as a weak acid, is the dominant form up to pH 9.1 (pK_{a1}). With further pH increase, $H_2AsO_3^-$ and $HAsO_3^{2-}$ become the dominant forms above 12.1 (pK_{a2}) and 13.4 (pK_{a3}), respectively.

The method described by Čerović *et al.* [42] was used for point of zero change (pH_{PZC}) determination of the investigated adsorbents. The obtained pH_{PZC} values were 6.6, 6.5 and 6.3 for Y00, Y05 and Y10, respectively. The increases of yttrium content slightly decreased pH_{PZC} of the adsorbents. These results indicate that below pH 6.4±0.2, the adsorbent surface would be positively charged, and at higher pHs, would be negatively charged. A similar pH_{PZC} value for magnetite was reported earlier in the literature [43].

The effect of pH (Fig. 8) on the adsorption of As(III) and As(V) was investigated using initial concentrations of As(III) and As(V) of 1000 μg/L in the pH range 2-12. The other adsorption parameters were previously defined above.

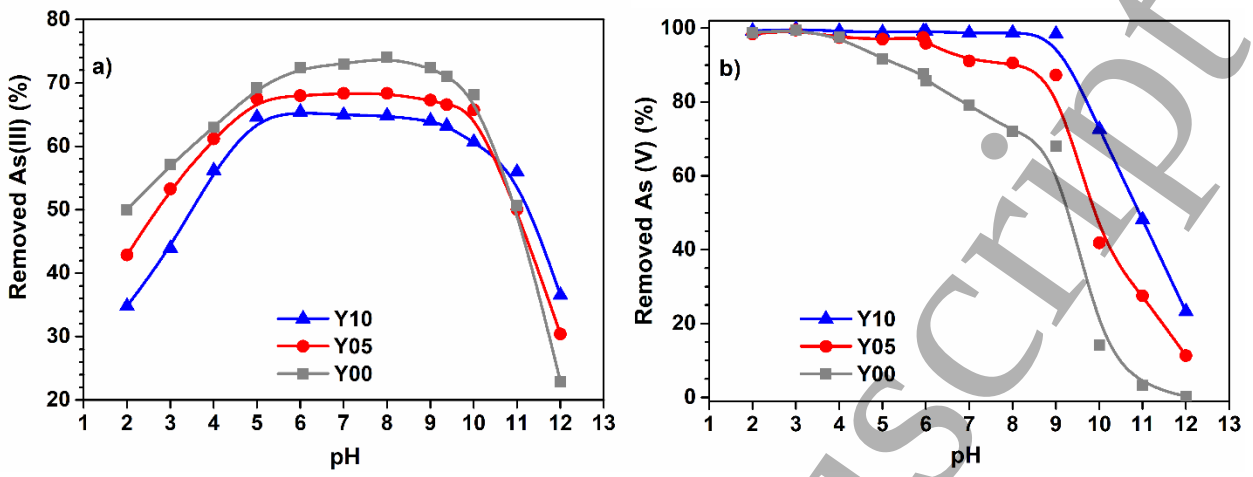

Fig. 8 The effect on initial pH on adsorption of a) As(III) and b) As(V) onto Y00, Y05 and Y10; (initial concentration As(III) or As(V) =1000 µg/L; adsorbents= 500 mg/L; ionian strength=0.01 M NaCl; time=120 min).

The adsorption of As(III) on all investigated adsorbents showed similar trends (Fig. 8a). The removal of As(III) increased with increasing initial pH of solution from 2-5, and then reached maximum and relatively constant removal within the pH range 5-10. With increasing of pH, the positive charge of adsorbents decreases and interaction between the surface and molecules of H_3AsO_3 is more dominant. Further pH increase, though, led to sharp decreases in the percentage of As(III) removed. This could be discussed from two aspects: (i) at pH>10 the adsorbents' surface charges were predominantly negative and repulsion with $H_2AsO_3^-$ anions was expected, and; (ii) the competition of hydroxyl anions with As(III) anion species for active adsorption sites increased with pH increase.

Results presented in Fig. 8b indicate that Y^{3+} concentration and morphology of adsorbents had high impacts on the pH range where the percentage of As(V) removal was almost 100%. The adsorption of As(V) on Y10 showed a wide pH range 2-9 with 100% of As(V) removal. With decreasing Y^{3+} content, the pH range with complete removal of As(V) became more narrow (pH 2-6 for Y05 and pH 2-4 for Y00). The removal of As(V) decreased when pH was above 9, 6 and 4 for Y10, Y05 and Y00, respectively. The decreased removal of As(V) at higher pH could be explained by similar factors as for As(III) removal: the predominantly negative surface charge of the adsorbent and competition reaction between $HAsO_4^{2-}/AsO_4^{3-}$ ions with hydroxyl anions, while it can be considered that the presence of yttrium in our magnetite structure is connected with stability and widening of the working pH range. In the cases of both arsenic species, a wider working pH range was obtaiend than was reported earlier in the literature

for $CoFe_2O_4$@MIL-100(Fe) hybrid magnetic nanoparticles [44]. The substitution of Fe^{3+} with Y^{3+} in magnetite had the most pronounced impact on As(V) adsorption using adsorbent Y10. On Y10, the maximum removal of As(V) was achieved in the widest pH range (pH 2-9). After adsorption onto Y10 under these conditions, the initial concentration of As(V) (1000 μg/L) was reduced to below 10 μg/L, which is the maximum permissible concentration of arsenic in drinking water as prescribed by the World Health Organization (WHO) as well as the U.S. Environmental Protection Agency (EPA). Such high concentrations of arsenic compounds (1000 μg/L) are found in groundwater in India and Bangladesh, while in Serbia (Vojvodina, Banat) and other areas in the world, groundwater concentrations are about 250 μg/L or lower. This load of arsenic compounds in groundwater worldwide indicates that use of an adsorbent based on our Y^{3+} substituted magnetite, Y10, could effectively eliminate arsenic species with minimal pre-treatment. Also, only at the extreme pH 2 was minimum leakage of yttrium and iron from the crystal lattice of nanomaterial Y10 measured (<2% m/m), while above pH 4, the leakage was <0.1% m/m. These data indicate the high stability of the nanomaterial Y10 when applied to arsenic removal from water. This is very important from the technological aspects and for the eventual application of adsorption material Y10. Another important feature of Y10 is the minimal disturbance of constituents in water during arsenic removal (see 3.5.3).

3.5.3. Competing agents

The effect of anions usually present in groundwater (humic acid sodium salt, sulphate and phosphate) on As(III)/As(V) adsorption using Y10, Y05 and Y00 was examined. The amounts of adsorbed As(III) and As(V) in the presence of anions are presented in Table S2.

It was observed that the presence of anions had an impact on adsorption of arsenic in both oxidative states. The results in Table S2 show that sulphate anions improved As(V) adsorption. The assumption for this finding is that sulphate and arsenate anions do not directly compete for the same adsorption site. Additional adsorption of As(V) could be ascribed to previously adsorbed SO_4^{2-} becoming new adsorption sites for As(V) adsorption. A similar explanation could be applicable for adsorption of As(V) in the presence of humic acids. The exception to the trend of improving As(V) adsorption in the presence of anions was observed only when Y05 was used as adsorbent. On the other hand, the presence of phosphate reduced As(V) adsorption to ~90% of the adsorption obtained for As(V) in media without additional anions.

The presence of sulphate anions and humic acid slightly decreased the amount of adsorbed As (III), but the observed decrease was less than 15%. On the other hand, the phosphate anions acted in the same manner as in the case of adsorption of As(V) and reduced the adsorption capability of all applied adsorbents, particularly Y10, where the presence of 5mM PO_4^{3-} reduced the adsorption of As(III) by more than 60%.

The effect of increased anion concentration for all investigated anions (SO_4^{2-}, PO_4^{3-}, HA) had almost negligible impact on the previously described trends.

4. Conclusion

To our best knowledge this is the first report in the literature on an integrated investigation of the impact of substitution of iron with yttrium ions on the morphology of magnetite-based nanoparticles. By maintaining constant conditions of co-precipitation synthesis and the same thermal treatment in a microwave field, and by changing only yttrium concentration, a significant effect of yttrium ions on the morphology of the formed samples is demonstrated. While Fe_3O_4 nanoparticles are mostly pseudospherical with relatively uniform size distribution, partial substituion of iron with yttrium leads to inhomogeneity in morphology: nanorods appear, as does a broader distribution of pseudospherical nanoparticles. With

increasing concentrations of yttrium, the quantity of nanorods increases, and aggregates of pseudospherical nanoparticles are formed. All samples produced exhibit porosity, with pore diameter sizes predominantly in the mesopore region. Results of a study of adsorption properties towards inorganic arsenic show the investigated nanomaterials have low adsorption capacity and slow arsenic adsorption kinetics, as other authors reported previously for iron oxide nanoparticles. These factors could be improved by design of composite with materials having better adsorption afinities and taking advantage of their superparamagnetic nature. However, the importance of our work for tailoring magnetite-based sorbents is the influence of morphology/ion substitution on inorganic arsenic(III) and arsenic(V) removal from water. Increased Y^{3+} content in $Fe_{3-x}Y_xO_4$ nanoparticles increases their adsorption capacity for As(V), significantly expands the optimum pH range for maximum As(V) removal, and decreases the contact time needed for such removal. Improved adsorption performance of $Fe_{3-x}Y_xO_4$ nanoparticles, achieved by increasing their yttrium content, is a very important result for the technology of purifying underground and wastewaters, and will be an important guideline for future reasearch in the area of designing magnetite-based nanoparticles for applications in waste water treatments and many other technologies.

Conflicts of interest

There are no conflicts to declare.

Acknowledgment

This work was supported by the European Commission through the Project MAGBIOVIN, Grant agreement #621375 and by the Ministry of Education, Science and Technological Development of the Republic of Serbia through the Eureka Project, E!9982 and Project's Grant Grants No. III45015 and OI 172030.

References

[1] Zhang Q, Liu J, Yuan K, Zhang Z, Zhang X and Fang X 2017 *Nanotechnology* **28** 405101

[2] Singh S, Barick K C and Bahadur D 2011 *Journal of Hazardous Materials* **192** 1539–47

[3] Bhuyan D, Arbuj S S and Saikia L 2015 *New J. Chem.* **39** 7759–62

[4] Yang C, Wu J and Hou Y 2011 *Chemical communications (Cambridge, England)* **47** 5130–41

[5] Blanco-Andujar C, Ortega D, Pankhurst Q A and Thanh N T K 2012 *J. Mater. Chem.* **22** 12498

[6] Zhen L, He K, Xu C Y and Shao W Z 2008 *Journal of Magnetism and Magnetic Materials* **320** 2672–5

[7] Wang J, Peng Z, Huang Y and Chen Q 2004 *Journal of Crystal Growth* **263** 616–9

[8] Podoliak N, Buchnev O, Bavykin D V, Kulak A N, Kaczmarek M and Sluckin T J 2012 *Journal of colloid and interface science* **386** 158–66

[9] Zhou W, Tang K, Zeng S and Qi Y 2008 *Nanotechnology* **19** 65602

[10] Zhang W, Jia S, Wu Q, Ran J, Wu S and Liu Y 2011 *Materials Letters* **65** 1973–5

[11] Wong W, Wong H Y, Badruzzaman A B M, Goh H H and Zaman M 2017 *Nanotechnology* **28** 42001

[12] Andjelkovic I, Stankovic D, Nesic J, Krstic J, Vulic P, Manojlovic D and Roglic G 2014 *Ind. Eng. Chem. Res.* **53** 10841–8

[13] Andjelkovic I, Nesic J, Stankovic D, Manojlovic D, Pavlovic M B, Jovalekic C and Roglic G 2014 *Clean Techn Environ Policy* **16** 395–403

[14] Gihring T M, Druschel G K, McCleskey R B, Hamers R J and Banfield J F 2001 *Environ. Sci. Technol.* **35** 3857–62

[15] van Genuchten C M, Addy S E A, Peña J and Gadgil A J 2012 *Environmental science & technology* **46** 986–94

[16] Kim J and Benjamin M M M M 2004 *Water research* **38** 2053–62

[17] Shipley H J, Yean S, Kan A T and Tomson M B 2009 *Environmental toxicology and chemistry* **28** 509–15

[18] Wang T *et al* 2013 *ACS applied materials & interfaces* **5** 12449–59

[19] Venkateswarlu S, Lee D and Yoon M 2016 *ACS applied materials & interfaces* **8** 23876–85

[20] Li Y, Liu J R, Jia S Y, Guo J W, Zhuo J and Na P 2012 *Chemical Engineering Journal* **191** 66–74

[21] Martinson C A and Reddy K J 2009 *Journal of colloid and interface science* **336** 406–11

[22] Yu Y, Yu L, Shih K and Chen J P 2018 *Journal of colloid and interface science* **521** 252–60

[23] Lin S, Lu D and Liu Z 2012 *Chemical Engineering Journal* **211-212** 46–52

[24] Feng L, Cao M, Ma X, Zhu Y and Hu C 2012 *Journal of Hazardous Materials* **217-218** 439–46

[25] Ognjanović M, Stanković D M, Ming Y, Zhang H, Jančar B, Dojčinović B, Prijović Ž and Antić B 2019 *Journal of Alloys and Compounds* **777** 454–62

[26] Rodríguez-Carvajal J 1993 *Physica B: Condensed Matter* **192** 55–69

[27] Juan Rodriguez-Carvajal and Thierry Roisnel 35–6

[28] Järvinen M 1993 *J Appl Crystallogr* **26** 525–31

[29] V. Honkimäki and P. Suortti *Effects of instrument function, crystallite size, and strain on reflection profiles*

[30] Louër D and Langford J I 1988 *J Appl Crystallogr* **21** 430–7

[31] Banković P, Milutinović-Nikolić A, Mojović Z, Jović-Jovičić N, Perović M, Spasojević V and Jovanović D 2013 *Microporous and Mesoporous Materials* **165** 247–56

[32] Žunić M J, Milutinović-Nikolić A D, Stanković D M, Manojlović D D, Jović-Jovičić N P, Banković P T, Mojović Z D and Jovanović D M 2014 *Applied Surface Science* **313** 440–8

[33] Jain R, Luthra V and Gokhale S 2016 *Journal of Magnetism and Magnetic Materials* **414** 111–5

[34] Shannon R D 1976 *Acta Cryst A* **32** 751–67

[35] Kremenović A, Antić B, Vučinić-Vasić M, Colomban P, Jovalekić Č, Bibić N, Kahlenberg V and Leoni M 2010 *J Appl Crystallogr* **43** 699–709

[36] Vučinić-Vasić M, Antic B, Kremenović A, Nikolic A S, Stoiljkovic M, Bibic N, Spasojevic V and Colomban P 2006 *Nanotechnology* **17** 4877

[37] Roisnel T and Rodríquez-Carvajal J 2001 *MSF* **378-381** 118–23

[38] Sing K S W 1985 *Pure and Applied Chemistry* **57** 603–19

[39] Sing K S W 1982 *Pure and Applied Chemistry* **54** 2201–18

[40] Wang J, Chen Q, Zeng C and Hou B 2004 *Adv. Mater.* **16** 137–40

[41] He K, Xu C-Y, Zhen L and Shao W-Z 2007 *Materials Letters* **61** 3159–62

[42] Čerović L S, Milonjić S K, Todorović M B, Trtanj M I, Pogozhev Y S, Blagoveschenskii Y and Levashov E A 2007 *Colloids and Surfaces A: Physicochemical and Engineering Aspects* **297** 1–6

[43] Yean S, Cong L, Yavuz C T, Mayo J T, Yu W W, Kan A T, Colvin V L and Tomson M B 2005 *J. Mater. Res.* **20** 3255–64

[44] Yang J-C and Yin X-B 2017 *Scientific reports* **7** 40955